Monthly Notices
of the
ROYAL ASTRONOMICAL SOCIETY

Mon. Not. R. Astron. Soc. **400,** 887–897 (2009) doi:10.1111/j.1365-2966.2009.15497.x

Molecular line profiles of collapsing gas clouds

Yang Gao,[1⋆] Yu-Qing Lou[1,3,4⋆] and Kinwah Wu[2⋆]

[1]*Department of Physics and Tsinghua Centre for Astrophysics (THCA), Tsinghua University, Beijing 100084, China*
[2]*Mullard Space Science Laboratory, University College London, Holmbury St. Mary, Surrey RH5 6NT*
[3]*National Astronomical Observatories of China, Chinese Academy of Sciences, A20, Datun Road, Beijing 100012, China*
[4]*Department of Astronomy and Astrophysics, The University of Chicago, 5640 South Ellis Avenue, Chicago, IL 60637, USA*

Accepted 2009 August 5. Received 2009 July 31; in original form 2008 November 15

ABSTRACT

Emission-line profiles of the tracer molecule H_2CO 140 GHz transition from gravitational core collapsing clouds in the dynamic process of forming protostars are calculated, using a simple ray-tracing radiative transfer model. Three self-similar dynamic inside-out core collapse models – the conventional polytropic model, the empirical hybrid model and the isothermal model – for star-forming molecular clouds are examined and compared. The isothermal model cannot produce observed asymmetric double-peak molecular line profiles. The conventional polytropic model, which gives flow velocity, mass density and temperature profiles self-consistently, can produce asymmetric double-peak line profiles for a core collapsing cloud. In particular, the blue peak is stronger than the red peak, consistent with a broad class of molecular line-profile observations. We find that line profiles are robust against variations in the polytropic index γ once the effective line-centre opacity κ_0 is specified. The relative strengths of the blue and red peaks within a molecular line profile are determined by the cloud temperature gradient, but the emission at frequencies between the two line peaks is determined by detailed density and velocity profiles in the cloud core. In the presence of a static dense kernel at the centre of a collapsing cloud, strong internal absorption along the line of sight may occur, causing a suppression to the red wing of the blue line peak. If reliably resolved in frequency by observations, this signature may be potentially useful for probing the environs of an infant protostar. The conventional polytropic model can be utilized to produce molecular line-profile templates, for extracting dynamical information from line spectra of molecular globules undergoing a gravitational core collapse. We show a sample fit using the 140 GHz H_2CO emission line from the central region of the molecular globule B335 by our model with $\gamma = 1.2$. The calculation of line profiles and fitting processes also offer a scenario to estimate the protostellar mass, the kernel mass accretion rate and the evolution time-scale of a core collapsing cloud. Our model can be readily adapted to other tracer molecules with more or less constant abundances in star-forming clouds.

Key words: hydrodynamics – line: profiles – radiative transfer – stars: formation – ISM: clouds – ISM: individual (Bok globule B335).

1 INTRODUCTION

How molecular clouds collapse to form protostars is an important question in modern astronomy and cosmology. Since hydrodynamic collapse models for star formations in molecular clouds were first proposed in the 1960s (e.g. Bodenheimer & Sweigart 1968; Larson 1969; Penston 1969), substantial progress has been achieved in modelling dynamic properties of core collapsing clouds (e.g. Hunter 1977; Shu 1977; Tsai & Hsu 1995; Fatuzzo, Adams & Myers 2004; Lou & Shen 2004; Shen & Lou 2004, 2006; Lou & Gao 2006; Hu & Lou 2008; Myers 2008; Evans et al. 2009; Lou & Zhai 2009). This progressive research advancement leads us to a more realistic understanding of the star formation processes in molecular clouds. In particular, the gas flow velocity, mass density and thermal temperature structures of collapsing clouds predicted by theoretical models are in principle testable by various high-resolution spectral imaging observations in different bands of tracer molecular line profiles (e.g. Snell 1981; Zhou et al. 1993; Mardones et al. 1997; Saito et al. 1999; Belloche et al. 2002; De Vries, Narayanan & Snell 2002; Yang et al. 2002; Evans et al. 2005).

A widely discussed scenario for the formation of low-mass protostars is the so-called inside-out collapse model (Shu 1977). In this

⋆E-mail: gaoyang-00@mails.tsinghua.edu.cn (YG); louyq@tsinghua.edu.cn (Y-QL); kw@mssl.ucl.ac.uk (KW)

model, a condensed cloud core becomes unstable gravitationally and collapses rapidly towards the centre to form a protostellar core. The protostar is embedded in a dusty envelope, which is presumed to be static, although in some variations of the model the envelope may also involve an infall or an outflow (e.g. Lou & Shen 2004; Shen & Lou 2004; Hu & Lou 2008; Lou & Zhai 2009). The boundary between the collapsing core and the envelope expands, engulfing more and more mass into the central collapsing core. The accretion of dusty materials from the envelope forms a disc rotating about the central protostar, and magnetized bipolar outflows may occur from the disc at the same time (e.g. Shu, Adams & Lizano 1987). The inside-out model has enjoyed supports from observations of some molecular globules. The Bok molecule globule B335 (e.g. Frerking, Langer & Wilson 1987; Zhou et al. 1993; Choi et al. 1995; Saito et al. 1999; Stutz et al. 2008) serves as a test example among others (e.g. Hogerheijde & Sandell 2000). However, there are features of line emissions from this star-forming cloud (see e.g. Wilner et al. 2000) and also observations of other cloud systems, such as IRAM 04191 (e.g. André, Motte & Bacmann 1999; Belloche et al. 2002) and L1544 (e.g. Tafalla et al. 1998; van der Tak, Caselli & Ceccarelli 2005), that are not readily explained by the *isothermal* inside-out collapse scenario as advanced by Shu et al. (1987).

Different from the inside-out collapse scenario for a molecular cloud, there are alternative models to describe the formation of low-mass protostars within molecular clouds, e.g. the isothermal Bonnor–Ebert sphere embedded in an external medium of finite pressure $P_{\rm E}$ (Ebert 1955; Bonnor 1956). This model describes the hydrostatic equilibrium of a gaseous sphere with a constant kinetic temperature, while a central core with finite density is involved. Such a hydrostatic sphere can be maintained as long as the mass of the cloud does not exceed the critical value of $M_{\rm c} = 1.18a^4/(G^{3/2}P_{\rm E}^{1/2})$, where a is the isothermal sound speed and G is the gravitational constant. With the density profile and kinetic temperature being the two key aspects, dynamic instability is predicted therein, but no flow velocity is presumed. Recent research shows that the hydrostatic Bonnor–Ebert sphere may match several observed properties of starless cores (e.g. Evans et al. 2001; Belloche et al. 2002; Myers 2005), while it cannot account for the observational data of the B335 source (see e.g. Harvey, Wilner & Myers 2003). This isothermal sphere model with a finite mass in a hydrostatic equilibrium cannot fully describe the observations of molecular line profiles in the cloud core because of the very isothermal assumption as we shall show in the following sections.

The Larson–Penston (LP) self-similar solution (Larson 1969; Penston 1969) of an isothermal sphere is a classic dynamic model for low-mass star formation. This LP-type model predicts the formation of stellar density cores around the centre of molecular clouds. Characteristically, the decreasing-towards-centre radial collapse speed profiles are obtained along with corresponding mass density profiles. However, the isothermal assumption encounters a similar problem of the Bonnor–Ebert sphere for modelling the observed molecular line profiles. Relaxing the dynamic self-consistency, all these models may be partially applied semi-empirically to star formation clouds for developing diagnostics. For example, recent empirical works make use of the millimetre continuum emission and provide empirical thermodynamic (density and temperature) profiles (e.g. Shirley, Evans & Rawlings 2002; Tafalla et al. 2002; Evans et al. 2005). These model results offer an independent perspective to probe star-forming clouds, but the overall dynamic profiles lack the desired self-consistency. In reference to these dynamic models, current observations and empirical works, the polytropic envelope expansion with core collapse (EECC) solution (e.g. Lou & Gao 2006; Gao & Lou 2009; Lou & Wang 2006; Wang & Lou 2008; Lou & Hu 2009) appears to be a sensible alternative. With radial velocity fields, corresponding density profiles and variable temperature profiles, this self-similar dynamic model should be more practical and versatile in explaining different observations (Lou & Gao 2006; Gao & Lou 2009). Molecular emission lines provide valuable observational diagnostics to probe the dynamics and physical conditions in star-forming clouds (e.g. Dyson & Williams 1997). For examples, optically thick emission lines of tracer molecules H_2CO, HCO^+, CO, CS and N_2H^+ are frequently identified for such diagnostic purposes. However, there are still unknown and uncertain parameters as well as model degeneracies to explain the line strengths and profiles, due to global hydrodynamics, macro- and micro-scale kinematics, thermal structures, chemical compositions and turbulence. It is thus important to resolve these issues step by step to avoid ambiguities in spectral modelling as well as in both observational and theoretical interpretations.

To date, most molecular line-profile calculations assume a certain parametrization for the density, velocity and temperature structures within emitting clouds. For example, in Zhou et al. (1993), the so-called exact theory takes the density and velocity profiles from the *isothermal* dynamic model of Shu (1977) but the temperature profile is assigned separately with a certain empirical base and therefore the gas cloud model is actually *non-isothermal* for molecular line calculations. This is a worthwhile attempt, yet such a specification of the radial temperature structure is unsatisfactory as there are inconsistencies in the velocity and density profiles of an *isothermal* cloud from the theoretical perspective. In recent years, calculations (e.g. De Vries & Myers 2005) considered more structural complexities in star-forming molecular clouds and invoked a more sophisticated radiative transfer model that incorporates the relevant atomic processes (e.g. Rawlings & Yates 2001; Ward-Thompson & Buckley 2001; Keto et al. 2004; Tafalla et al. 2006; Pavlyuchenkov et al. 2008; Tsamis et al. 2008). These studies aimed at resolving specific issues, such as the chemical profiles (e.g. Rawlings & Yates 2001; Tsamis et al. 2008) or the competition between relevant atomic processes (e.g. Pavlyuchenkov et al. 2008). As the effects of dynamical and thermal structures were not their prime objective, most of these calculations basically parametrized the density, velocity and temperature structures in a collapsing cloud or simply adopted the isothermal inside-out collapse model of Shu (1977) but took an empirical temperature profile from observations of dust continuum.

The key question now is: does it make a difference if the structure profile of a cloud is determined self-consistently through a polytropic hydrodynamic model analysis instead of using a simple isothermal inside-out model but with a non-isothermal temperature profile? Also, are the molecular line profiles different for models with different polytropic indices of the gas dynamics? These questions are essential for our understanding of the dynamics and physical conditions, in particular, in the early stage of forming low-mass protostars. The objective of our study here is to address this issue quantitatively. For instance, we calculate H_2CO 140 GHz molecular line profiles using a self-similar hydrodynamic model that involves a conventional polytropic equation of state (EoS; Fatuzzo et al. 2004; Lou & Gao 2006; Lou & Wang 2006; Hu & Lou 2008; Wang & Lou 2008; Gao & Lou 2009) and an isothermal inside-out collapse model (Shu 1977), and carefully compare their differences. We also directly compare the H_2CO 140 GHz molecular line profiles obtained from the conventional polytropic model (Lou & Gao 2006) with observations, using the molecular cloud B335 as a test example. Comparison of our theoretical approach with empirical approaches

used in former works is also made. In principle, our model calculations can be readily adapted to line profiles of tracer molecules of more or less constant abundances in star-forming clouds.

This paper is structured as follows. In Section 2, we present model structures of conventional polytropic and isothermal inside-out collapse models with their flow velocity, density and temperature profiles. The relevant parameters and scalings of dynamic models are also specified there. We provide an overview for the formation of molecular line profiles in star-forming clouds in this section. In Section 3, we present the results of calculations, the comparison of the lines obtained by dynamical models and the comparison of the theoretical with the observed molecular line profiles. Effects due to the cloud temperature gradient, optical depth, intrinsic linewidth, polytropic index and the presence of a relatively dense central kernel are also considered. Finally, results of our analysis are summarized in Section 4. For the convenience of reference, we summarize the basic polytropic hydrodynamics and the relevant asymptotic self-similar solutions in Appendix A, elaborate on how the blue and red peaks of a molecular line profile are shaped in an optically thick cloud in Appendix B and lay out the radiative transfer formulation and our ray-tracing computation algorithm in Appendix C.

2 SELF-SIMILAR HYDRODYNAMIC MODELS

Three self-similar hydrodynamic models for the velocity, density and temperature profiles are considered in our molecular line-profile calculations, namely Model I, a hydrodynamic collapse model with a conventional polytropic EoS for the gas (Hu & Lou 2008; Lou & Gao 2006); Model II, an isothermal inside-out collapse model (Shu 1977); and Model III, an empirical hybrid model (Zhou et al. 1993).[1] In all these three models, the molecular cloud consists of a free-fall collapsing inner core and a static outer envelope. A self-similar dynamic solution is adopted for the collapsing core in both Models I and II. For Model I, we further use three specialized solutions for comparison. In fact, the isothermal case (Model II) can be regarded as a very special case of the conventional polytropic model (Model I) with $\gamma = n = 1$.

2.1 Parameters of hydrodynamic model solutions

Details of Model I and relevant asymptotic solutions are contained in Appendix A for reference. Model I is characterized by $n + \gamma = 2$, where n is a scaling index for polytropic self-similar hydrodynamics and γ is the polytropic index (see Appendix A; Lou & Gao 2006; Lou & Wang 2006; Hu & Lou 2008). We choose different dynamic solutions with a static outer envelope and free-fall inner core collapse for comparison in terms of tracer molecule line profiles. The density, velocity and temperature profiles can be directly derived from equations (A9), (A10) and (A7) for a conventional polytropic gas dynamics under self-gravity.

For conventional polytropic solutions with $\gamma = 1.1$, 1.2 and 1.3, the corresponding values of the dimensionless infall radius x_0, the dimensionless core mass m_0, and coefficients A and B for asymptotic solution (A12) are contained in Table 1. Parameters for the isothermal model of $\gamma = n = 1$ are also listed in Table 1. In our solutions constructed with static singular polytropic solution (SPS) envelopes, the dimensionless infall radius x_0 depends on n only and is analytically given by

$$x_0 = \frac{(2-n)^{1/2}}{n}[2(3n-2)]^{(1-n)/2} . \quad (1)$$

The velocity parameter B of an asymptotic solution for the static envelope vanishes and the mass parameter A can be derived:

$$A = \left[\frac{2(3n-2)(2-n)}{n^2}\right]^{1/n} , \quad (2)$$

which is exactly the same as the coefficient of $\alpha(x)$ in SPS solution (A11). The dimensionless central point mass m_0 of asymptotic free-fall solution (A13) is then determined numerically. Fig. 1 shows parameter variations of x_0, A and m_0 as the scaling index γ (or equivalently $n = 2 - \gamma$) varies continuously. This is in fact the case [i.e. expansion-wave collapse solution (EWCS)] of a static SPS envelope connected with a free-fall collapsing core and is much more general than the special isothermal case of Shu (1977).

The dimensionless variables are converted to corresponding dimensional physical variables in order to perform radiative transfer calculations for molecular line profiles in core collapsing clouds. We adopt parameter values estimated from observations for the scalings of the dynamic profiles for model clouds. The typical infall radius within a molecular cloud is estimated as $\sim$0.01–0.03 pc (e.g. Myers 2005), corresponding to $\sim 10^3$–10^4 au. As dimensionless infall radii are roughly around and larger than $x_0 = 1$ in our model (e.g. $1 \lesssim x_0 \lesssim 1.4$ by Fig. 1 and Table 1), we may choose the

Table 1. Parameters of self-similar polytropic dynamic solutions.

γ	n	x_0	m_0	A	B
1.0	1.0	1.00	0.975	2.00	0
1.1	0.9	1.17	1.25	2.04	0
1.2	0.8	1.35	1.15	1.66	0
1.3	0.7	1.28	0.26	0.40	0

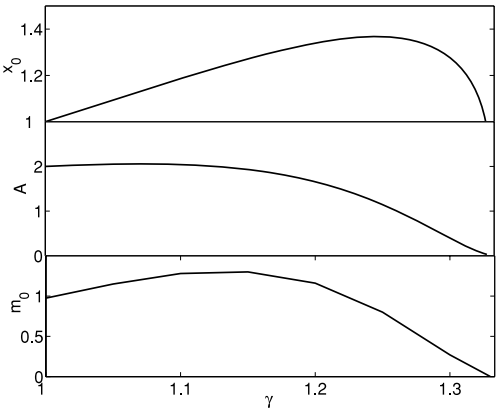

Figure 1. Parameter variations as functions of the polytropic index $\gamma = 2 - n$ for the expansion-wave collapse scenario with static SPS outer envelopes and dynamic free-fall cores as in Model I. The upper panel is the infall radius x_0, the middle panel is the mass parameter A given by equation (2) for SPS solution (A11) and the bottom panel is the point mass m_0 for $x \to 0^+$. Consistently, $\gamma = 1$ is the isothermal case (Model II) with parameters $x_0 = 1$, $A = 2$ and $m_0 = 0.975$. All these parameters increase slightly and then fall as γ increases from 1 to $(4/3)^-$. The special case of $\gamma = 4/3$ ($n = 2/3$) is investigated by Lou & Cao (2008) and Cao & Lou (2009).

[1] The hybrid model of Zhou et al. (1993) takes the mass density and flow velocity profiles from the isothermal model of Shu (1977) and uses an empirical variable temperature profile. This empirical temperature profile was inferred based on an isothermal density profile which scales as r^{-2}.

following length-scale

$$k^{1/2}t^n = 10^4 \text{ au} \tag{3}$$

in definition (A5). A typical number density at the infall radius is $\sim 10^4\,\mathrm{cm}^{-3}$ (e.g. Harvey et al. 2003; Evans et al. 2009). For the mass parameter $A \lesssim 2$ as shown in Fig. 1, the reduced number density being of the order of unity implies a proper number density scale as (see equation A6)

$$1/\left(4\pi G\mu m_{\rm H} t^2\right) \cong 10^4\,\mathrm{cm}^{-3}\,. \tag{4}$$

This corresponds to a thermal temperature of $T \sim 4$ K by equation (A7) and a characteristic infall age of $t \sim 3 \times 10^5$ yr by equation (4) for a molecular cloud (see e.g. Myers 2005). Within the infall radius, this scaling also gives an enclosed mass scale of $M \simeq 0.5\,\mathrm{M}_\odot$ and a sound speed scale of $c \simeq 0.15\,\mathrm{km\,s}^{-1}$ by equations (A6) and (A8). In addition to the central protostar, we presume a number density of $\sim 10^6\,\mathrm{cm}^{-3}$ at the very central region (i.e. $R \lesssim 500$ au) of a molecular cloud and set the central velocity to be zero for a static dense kernel. The outer cloud radius is set to be several tens of 10^3 au. We note that the size of the static dense kernel and the outer radius of the cloud are not the same as used in some previous works (e.g. Harvey et al. 2003; Evans et al. 2005; Myers 2005). The key parameter in our radiative transfer calculations is the effective optical depth of a molecular line in a cloud. Once the numerical value of the optical depth along the ray is specified, the actual size of an emitting cloud would be irrelevant. In this sense, the difference between cloud sizes used in our model analysis and those of earlier research works should not affect our basic conclusions. Nevertheless, we should keep in mind that this conclusion is made under the assumption that the abundance of tracer molecule remains constant in our model consideration. The cloud sizes would matter if the fractional abundances of certain tracer molecules vary considerably in star-forming clouds.

For comparison, the velocity, number density and temperature profiles of the three different models that we use in radiative transfer calculations of molecular line profiles are shown in Fig. 2. In all models, the velocity and density increase monotonically towards the centre until $R \approx 500$ au. There are slight differences between the density and velocity profiles of Model I ($\gamma = 1.2$) and Model II. The infall radii for Model II and Model I ($\gamma = 1.2$) are at $R = 10 \times 10^3$ and 13.5×10^3 au, respectively. While the temperature profiles of the three models are readily distinguishable. Model II has a flat constant temperature, Model I ($\gamma = 1.2$) has a monotonic increase in temperature towards the centre and Model III has a semi-empirical profile in which the temperature drops slightly from $R = 30 \times 10^3$ au to $R \approx 6 \times 10^3$ au and then increases when R decreases further. We also show in Fig. 3 the velocity, density and temperature profiles for Model I with different polytropic indices: $\gamma = 1.1$, 1.2 and 1.3, whose infall radii are at $R = 11.7 \times 10^3$, 13.5×10^3 and 12.8×10^3 au, respectively. As shown, cloud structures can vary substantially even within Model I (in fact, Model II can be regarded as a special case of Model I), and such differences can leave signatures in the emission molecular line profiles as expected.

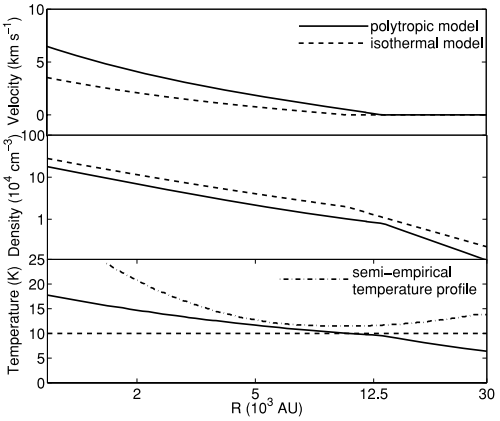

Figure 2. Inwards radial flow velocity, number density and thermal temperature profiles (panels from top to bottom, respectively) of three different model molecular clouds used in our molecular line-profile calculations. The abscissa represents the radius R in the unit of 10^3 au, shown on a logarithmic scale. The solid curves denote Model I with $\gamma = 1.2$; the dashed curves denote Model II. The dash–dotted curve in the bottom panel denote Model III, whose radial velocity and number density have the same manner as Model II (dashed curves in the top and middle panels). Other relevant model parameters can be found as $\gamma = 1.0$ for Models II and III, and $\gamma = 1.2$ for Model I in Table 1. The dimensional scalings used are described in Section 2, giving infall radii of $R = 10 \times 10^3$ au for Models II and III and $R = 13.5 \times 10^3$ au for Model I ($\gamma = 1.2$).

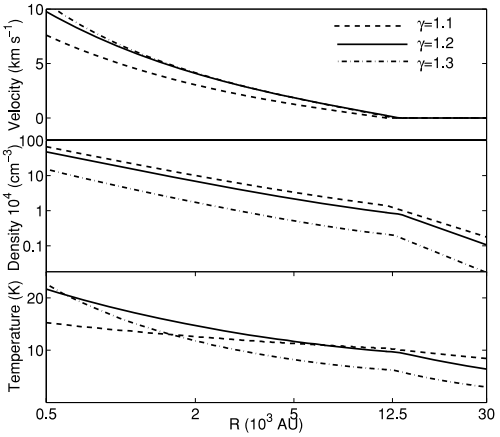

Figure 3. Inwards radial flow velocity, number density and thermal temperature profiles (panels from top to bottom, respectively) of Model I with three different polytropic indices γ. The dashed, solid and dash–dotted curves represent $\gamma = 1.1$, 1.2 and 1.3 with infall radii at $R = 11.7 \times 10^3$, 13.5×10^3 and 12.8×10^3 au, respectively. The corresponding central mass points are 1.13, 1.02 and $0.24\,\mathrm{M}_\odot$. Other relevant polytropic model parameters are contained in Table 1 and the physical scalings are described in Section 2. The case of $\gamma = 1.2$ is the same as shown in Fig. 2. A larger γ provides steeper density and temperature increases towards the centre; this effect will manifest in the corresponding H_2CO 140 GHz line profiles as discussed in Section 3.3.

2.2 A molecular line-profile calculation

We utilize a simple ray-tracing radiative transfer model (which does not involve an explicit treatment of atom and molecular transitions and their couplings with the radiation field; see Appendix C for details) to calculate the spectral profile of the molecule H_2CO (2_{12}–1_{11}) emission line at a frequency of 140 GHz. As the range of temperature variation in a cloud region is typically small (e.g. $\sim$10–20 K), the variation in tracer molecular level populations is small and thus will affect line profiles little (e.g. Tsamis et al. 2008).

It has been argued that gradients in distributions of chemical elements as well as chemical evolution are important in determining the strengths and profiles of molecular emission lines from star-forming clouds (e.g. Rawlings & Yates 2001; Pavlyuchenkov et al. 2008; Tsamis et al. 2008). As we focus on the effect of dynamical cloud structures on tracer molecule line profiles, the H_2CO

abundance is taken to be approximately constant in our model calculations. This simplification implies that our approach may be extended to those tracer molecules with more or less constant abundances in star-forming clouds. This assumption of constant abundance was invoked in some earlier works (e.g. Zhou et al. 1993; Ward-Thompson & Buckley 2001), while in others, the H_2CO abundance in the B335 cloud was assumed to be a step function with a variation of $\sim$10 times (e.g. Evans et al. 2005). In fact, recent empirical works based on observations do show that several diagnostic tracer molecules (e.g. HO, H_2CO, CN, CS) keep their abundance variations less than a factor of $\sim$10 (e.g. fig. 3 in Tsamis et al. 2008). Both theoretically and observationally, clarifications of the relative importance of dynamical and chemical effects are essential in using molecular line profiles as a reliable diagnostic probe into the core collapse dynamics in star-forming clouds. A more comprehensive description of star-forming clouds should involve self-consistent dynamic profiles and chemical abundance profiles that are independently inferred from observations.

In order to have an intuitive feeling for our model approach, we demonstrate in Appendix B how the blue and red peaks of emission molecular line profiles are formed in an optically thick cloud. The radiative transfer analysis and the computing algorithm of our line-profile calculations are described in Appendix C. The physical variables (i.e. temperature T, mass density ρ, projected velocity component v_p etc.) of a core collapsing molecular cloud are determined from our polytropic hydrodynamic model (see Appendix A). The line-centre opacity κ_0 and the linewidth Δv are set to values typical of spectral line observations of tracer molecules. In equations (C1)–(C4), the mass density ρ is mainly that of the interstellar medium in a cloud. As a consequence, the ratio of molecular abundance is merged into the parameter κ_0, which is then effectively a product of molecular line-centre opacity and its mass fractional ratio.

A simple assumption of local thermodynamic equilibrium (LTE) is made for the radiative transfer calculation; this calculation does not account for scattering dominated processes, masers, or other non-LTE cases.

3 RESULTS AND ANALYSES

3.1 Temperature variations in molecular clouds

It is clear that Model II does not produce asymmetric double-peak H_2CO 140 GHz line profiles (see the dashed curves in Fig. 4 and equations B3 and B4 in Appendix B), an apparent contradiction to extensive line-profile observations in molecular globules. Therefore, unless compromising the self-consistency in the thermal structure and dynamics to insert a semi-empirical temperature profile to replace the isothermal model, as in Model III, one cannot have a sensible comparison between the observed asymmetric double-peak line profiles of star-forming clouds and the line profiles calculated from Model II. In fact, equation (B4) in Appendix B clearly demands that the temperature should increase towards the cloud centre in order to produce a molecular line profile with a blue peak being stronger than the red peak for a core collapsing cloud. Fig. 4 (see also fig. 9a of Zhou et al. 1993) demonstrates that asymmetric molecular line profiles with a stronger blue peak emerge when Model III and Model I ($\gamma = 1.2$) are actually introduced. Recent radiative transfer works use empirical temperature profiles derived from the sub-millimetre continuum emission intensity are able to produce the observed asymmetric line profiles (e.g. Ward-Thompson & Buckley 2001; Evans et al. 2001; Tsamis et al. 2008).

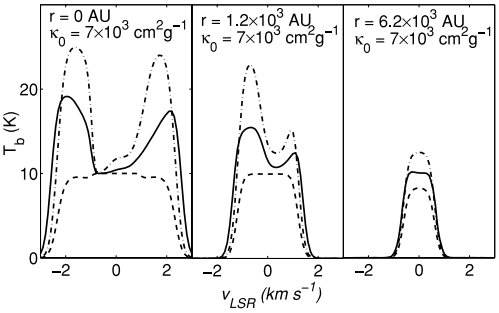

Figure 4. Profiles of H_2CO 140 GHz emission lines in terms of brightness temperature T_b from molecular clouds for Model I with $\gamma = 1.2$ (solid curves), Model II (dashed curves) and Model III (dash-dotted curves). The radial flow velocity, particle number density and thermal temperature profiles of the underlying dynamic models are shown in Fig. 2 with a central kernel to avoid the singularity. The intrinsic linewidths Δv are set to be $\sim$0.3 km s^{-1} here. Panels from left to right correspond to line emission profiles along the line of sight passing through $R = 0$ au, $R = 1.2 \times 10^3$ au and $R = 6.2 \times 10^3$ au, respectively. The effective total line-centre opacity is $\kappa_0 = 7 \times 10^3$ cm^2 g^{-1} in all three panels.

However, self-consistency of the dynamic profiles should be demanded for a more satisfying model construction.

We emphasize that the temperature profile is determined simultaneously once we derive mass density and flow velocity profiles from conventional polytropic hydrodynamic equations. Instead, when one uses an empirical temperature profile for molecular line-profile calculations, this empirical temperature profile and the density and velocity profiles are generally not consistent with each other in the hydrodynamic and thermodynamic sense. In other words, a gas cloud with dynamic profiles having no self-consistency does not exist according to hydrodynamics and thermodynamics. It should be also noted that the inference of empirical temperature profiles must also rely on several assumptions. Our goal is to develop theoretical models grossly satisfying available observational constraints.

Our calculations show that in both Model I ($\gamma = 1.2$) and Model III, the asymmetry in line profiles can be more pronounced in the off-centre region in a cloud, provided the ray of emission along the line-of-sight passes through the collapsing core of the cloud (compare the left-hand and middle panels of Fig. 4). The relative strengths of the blue and red peaks in a molecular line profile show a stronger contrast in Model III than in Model I ($\gamma = 1.2$). This sharper contrast in two peaks from Model III is due to the fact that there are more variations in the specified semi-empirical temperature profile than those in the temperature profile of Model I ($\gamma = 1.2$) that we adopt. Model II produces symmetric single-peak molecular line profiles in the resolved spectra by our numerical explorations (see three dashed curves of Fig. 4), while Model I ($\gamma = 1.2$) and Model III could produce single peak line profiles when the rays are along the line-of-sight passing through only the static outer envelope or when velocity variations are insignificant in the emission region as compared with the intrinsic velocity broadening Δv of H_2CO 140 GHz line.

3.2 Line opacity and intrinsic velocity width

The left-hand panel of Fig. 5 shows how the two peaks in H_2CO 140 GHz line profile vary with the value of the line-centre opacity κ_0. With density distribution being fixed, the opacity κ_0 characterizes the optical depth along the ray parallel to the line of sight. For forming asymmetric blue and red peaks, molecular line profiles

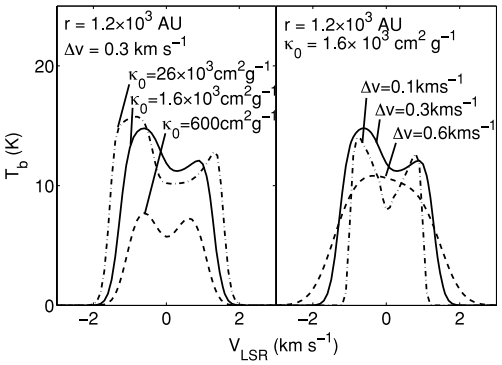

Figure 5. Profiles of H_2CO 140 GHz emission lines in terms of brightness temperature T_b from molecular clouds at $R = 1.2 \times 10^3$ au for Model I of $\gamma = 1.2$ with different values of the effective line-centre opacity $\kappa_0 = 0.6 \times 10^3$, 1.6×10^3, 2.6×10^4 cm^2 g^{-1} (left-hand panel) and for different values of intrinsic linewidths Δv (0.1, 0.3 and 0.6 km s^{-1}) with a fixed $\kappa_0 = 1.6 \times 10^3$ cm^2 g^{-1} (right-hand panel). Unless otherwise stated, the parameters adopted are the same as those in Model I in Fig. 2.

need to be optically thick, in addition to the presence of variable temperature and velocity structures within molecular clouds involving gravitational core collapse. For molecular lines that are optically thin, the observed emissions sample the entire collapsing core. A cloud structure of spherical symmetry for the near and far hemispheres inevitably gives rise to symmetric molecular line profiles, in spite of the temperature, density and velocity variations in the emission region. Moreover, as the line is optically thin, the line intensity is well below the source Planck function. Hence the line intensity becomes weaker, i.e. the corresponding brightness temperature is lower than the thermal temperature of line emission regions (see equation B.4 and discussions thereafter for an intuitive explanation for the formation of a double-peak line profile).

For comparisons of dynamic models, we have adopted that the intrinsic linewidth $\Delta v = 0.3\,\mathrm{km\,s^{-1}}$. There are uncertainties in the values of Δv and we have chosen a typical value here. It is generally believed that the intrinsic width of a molecular line is mainly caused by thermal broadening and micro-turbulence. The thermal broadening is estimated to be at a level of $\sim$0.1 km s^{-1} for a typical molecular cloud with a thermal temperature of $\sim$10 K. The turbulent broadening is fairly uncertain. Theoretical estimates depend on the assumed driving mechanisms (e.g. MacLow 1999; Li & Nakamura 2006; Matzner 2007). Some observational studies (e.g. Larson 1981) show that the probable linewidth Δv ranges from a few $\sim$0.1 km s^{-1} to about several km s^{-1}.

Typically, infall velocities v in cloud cores would range from $\sim$0.1 km s^{-1} to a few km s^{-1}, as adopted in the dynamic models explored here. The characteristic double-peak signature of molecular line profiles from a collapsing cloud may be erased or smeared if the line suffers a severe turbulent broadening (i.e. large Δv). The right-hand panel of Fig. 5 demonstrates that for Model I ($\gamma = 1.2$) with a maximum infall velocity of $\sim$2 km s^{-1}, we can produce a double-peak line profile for $\Delta v \lesssim 0.3\,\mathrm{km\,s^{-1}}$ but not for $\Delta v \gtrsim 0.6\,\mathrm{km\,s^{-1}}$. Extensive observations of double-peak line profiles in many molecular globules imply that the turbulence in their line formation region should not give rise to velocity broadenings significantly larger than $\sim$0.3 km s^{-1} with a maximum infall velocity $\sim$2 km s^{-1}. By a further numerical exploration, we find that the maximum allowed velocity broadening bears a linear relationship with the maximum infall speed; the values shown here are typical for star-forming clouds.

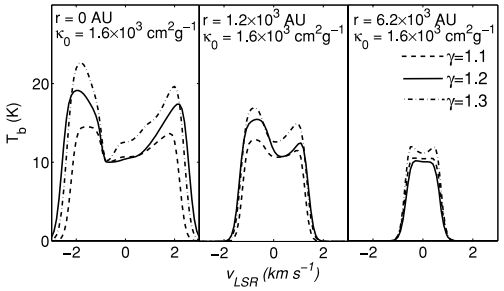

Figure 6. Profiles of H_2CO 140 GHz emission lines in terms of brightness temperature T_b from molecular clouds for the three polytropic models shown in Fig. 3. The dashed curve corresponds to the model with $\gamma = 1.1$, the solid curve to the model with $\gamma = 1.2$ and the dash-dotted curve to the model with $\gamma = 1.3$. The scale free infall radii are at $x_0 = 1.18$, 1.35 and 1.27, respectively. For all three panels, $\Delta v = 0.03\,\mathrm{km\,s^{-1}}$, $\kappa_0 = 7 \times 10^3$ cm^2 g^{-1}.

3.3 Polytropic index γ

One appealing aspect of Model I is that we can obtain self-consistent velocity, density and temperature profiles for molecular clouds within the overall inside-out collapse scenario. The essence of this model is the conventional polytropic EoS characterized by a polytropic index γ. The special isothermal case (Model II) just corresponds to $\gamma = n = 1$. Now our question is: how robust is the molecular line-profile morphology with respect to the variation of γ?

We calculate H_2CO 140 GHz emission-line profiles using Model I with three different polytropic indices $\gamma = 1.1$, 1.2 and 1.3, respectively. These γ values are representative of astrophysical situations between limiting regimes, e.g. the isothermal process of $\gamma = 1$, and the adiabatic processes of $\gamma = 7/5$ and $5/3$ for diatomic and monoatomic gases respectively. We found that the overall morphology of molecular line profiles is quite robust with respect to variations of γ, provided that the effective line-centre opacities in the calculations take on the same values (see Fig. 6). Note that $n + \gamma = 2$ for a conventional polytropic gas, i.e. a variation of γ leads to a variation of n, which is related to the scalings of hydrodynamic variables. There are however some small and subtle differences among predicted molecular line profiles. For instance, larger γ tends to give more prominent peaks in a line profile, which can be attributed to a much steeper gradient in the temperature increase towards the cloud centre (Fig. 3). Also, for a larger γ value, the molecular line peaks persist to larger projected radii away from the cloud centre (see the right-hand panel of Fig. 6). Nevertheless, these differences might not be readily distinguishable in observations, given the beam smearing in the spectral imaging observations and the presence of various noises in molecular line spectra.

3.4 The effect of a high-density central kernel

In theoretical models of gravitational core collapsing clouds, a static central dense kernel is introduced to avoid the singularity. Phenomenologically, the radius of the kernel marks the interface of an 'embryo' stellar kernel with the accreting gas in a gravitational free fall. This high-density kernel is more a theoretical hypothesis as was used in former works (e.g. Choi et al. 1995; Myers 2005) but it does fit the observed sub-millimetre intensity profile well (e.g. Evans et al. 2001).

The static high-density kernel could leave indelible signatures in molecular line profiles from the central core of a collapsing

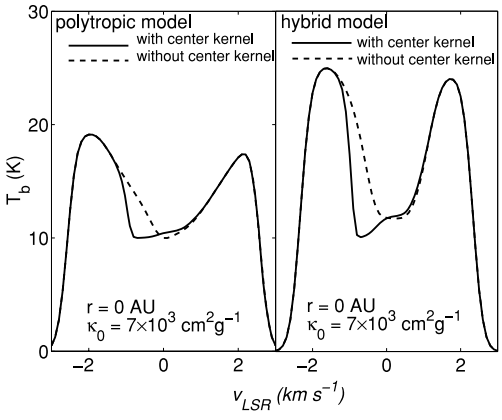

Figure 7. Comparison of H_2CO 140 GHz emission-line profiles in terms of the brightness temperature T_b along the line of sight passing through the cloud centre for Model I ($\gamma = 1.2$) (left-hand panel) and Model III (right-hand panel). The difference between the two model curves within each panel is that the solid curve is the same as the cloud as in Fig. 2 and the dashed curve has the innermost zero-velocity condensed kernel removed. Other parameters of the 'kernel-less' model clouds are the same as those in Model I and Model III in Fig. 2. In both panels, $\Delta v = 0.3$ km s^{-1}, $\kappa_0 = 7 \times 10^3$ cm^2 g^{-1}.

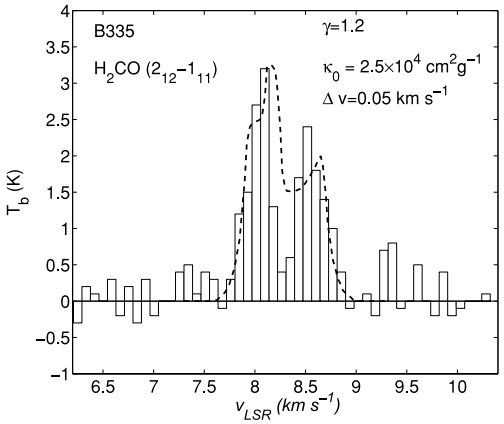

Figure 8. Comparison of the 140 GHz H_2CO (2_{12}–1_{11}) line profile towards the central region of the Bok molecular globule B335 with the theoretical molecular line profile obtained by Model I with $\gamma = 1.2$ (dashed line). The intrinsic line broadening is $\Delta v = 0.05$ km s^{-1} and the line-centre opacity is $\kappa_0 = 2.5 \times 10^4$ cm^2 g^{-1}. The radial receding displacement velocity of the entire cloud is $v_d \sim 8.30$ km s^{-1}. The infall speed is $\sim$0.8 km s^{-1} at a radial distance of $\sim 10^3$ au away from the cloud centre. The gas temperature of the central kernel is $\sim$10.0 K.

cloud. As the effective kernel opacity is large, molecular emissions from the far side (i.e. behind the dense kernel) would suffer strong absorptions at the rest-frame line-centre frequencies, depending on intrinsic line broadening Δv. In contrast, molecular emissions from the near side (i.e. in front of the dense kernel) are unaffected by the kernel. This naturally leads to the suppression of the red wing of the blue line peak. In the left-hand panel of Fig. 4, molecular line profiles manifest a dip feature in the red wing of the blue peak when the line of sight passes through the dense kernel. For rays along the lines of sight that avoid this central dense kernel, this dip feature would disappear (see the middle panel of Fig. 4 as an example). Fig. 7 compares molecular line profiles from both Models I ($\gamma = 1.2$) and III with and without a central kernel. The difference in molecular line profiles for the case with and without the dense static kernel is not negligible. Moreover, the presence of a dip makes the red peak appear broader than the blue peak. However, this difference in line profiles is similar to the difference caused by different values of γ in Model I (the left-hand panel of Fig. 6), as well as the difference between Model I and Model III (the left-hand panel of Fig. 4). So the actual cause of this phenomenon on profiles can only be solved after testing the temperature and density profiles of the cloud by some other means (e.g. the millimetre continuum).

Potentially, such a line feature may be utilized to probe the 'embryo' kernel surrounding a protostar in its development and evolution [e.g. pre-protostellar cores (PPCs) with detectable dust continuum emission at millimetre and sub-millimetre wavelengths] before the eventual emergence as a 'fully functional' star of nuclear burning. However in reality, whether or not such dips may be unambiguously resolved in the observed line profiles from molecular globules is determined by a few factors. In particular, it depends on the spectral resolution actually achieved by observations.

3.5 Comparisons with observed line profiles

It is straightforward that self-similar solutions of Model I combined with radiative transfer calculations (Appendix C) can be applied to fit observed H_2CO 140 GHz line profiles. Empirical estimates of physical variables at certain epochs are introduced for calibration and profiles of variables are derived from Model I self-consistently. As an example of illustration, we specifically model the 140 GHz H_2CO emission line from the Bok molecular globule B335. We take the observed line profile from Zhou et al. (1993), where the line emission was extracted along the line-of-sight path towards the cloud centre. The collapsing core (i.e. the infalling region around the centre) radius is $\sim$30 arcsec according to Zhou et al. (1993). By adopting an estimated distance of $\sim$250 pc to the Bok globule B335 (Tomita, Saito & Ohtani 1979), this gives a radius of $\sim 7.5 \times 10^3$ au for the infalling region. However, the uncertainty in this distance to B335 is fairly large (see table 2 of Tomita et al. 1979) and this radius may vary by more than a factor of 2. We take this radius to be $\sim 1 \times 10^4$ au for the collapsing core in our model calculations for the B335 cloud.

The same $\gamma = 1.2$ solution of Model I as in Fig. 2 is used to model the structure of a molecular line formation region. In order to achieve a reasonable fit with the observed molecular line profile, the density scale (4) is adjusted to $1/(4\pi G \mu m_H t^2) \cong 0.4 \times 10^4$ cm^{-3}, while the length scale (3) remains unchanged. Scalings of other parameters are adjusted accordingly. The radio telescope beam width of 17 arcsec (e.g. Zhou et al. 1993) is taken into account, i.e. molecular line profiles computed are spatially averaged over a projected area of 17×17 arcsec^2 and the resulting averaged molecular line profile is then compared with the observed profile. The maximum infall velocity is taken to be $\sim$1.49 km s^{-1} at 0.6×10^3 au and the radial receding displacement velocity v_d of the entire B335 cloud is $\sim$8.30 km s^{-1}. The intrinsic width of the molecular line is $\sim$0.05 km s^{-1} and the effective line-centre opacity is $\kappa_0 = 2.5 \times 10^4$ cm^2 g^{-1}. We find that a dense static inner kernel is needed in order to produce line profiles similar to the observed profiles. The kernel radius is $\sim 0.5 \times 10^3$ au and the mean particle number density in the kernel is $\sim 10^6$ cm^{-3}. Fig. 8 compares the observed line profile and the line profile produced by Model I ($\gamma = 1.2$). The good agreement between our model line profile and the observed line profile clearly shows the viability of the conventional polytropic hydrodynamic model and the applicability of our line-profile radiative transfer calculations.

It is possible to derive the central point mass M_0 and the total enclosed mass contained within the central kernel region $M_{\rm k}$ in Model I used in the above data fitting. Using the m_0 value (see Table 1 and Fig. 1) and scaling relations for our dynamic model with self-similar transformation (A6), we obtain the value of central point mass $M_0 = 0.410\,{\rm M}_\odot$, referred to as an estimate for the mass of the central protostar; this estimate is similar to the value of Zhou et al. (1993) and Stutz et al. (2008) and is $\sim$4 times larger than the mass value estimated by Saito et al. (1999). When we use the reduced enclosed mass $m(x)$ at the boundary of the central kernel, the dimensional enclosed mass contained within the kernel region is derived to be $M_{\rm k} = 0.411\,{\rm M}_\odot$. Estimates of all these masses are not sensitive to the kernel radius but are mainly affected by the variation in the infall radius. Therefore, all these masses would have an uncertainty of a few times. It is also possible to derive the mass accretion rate in the periphery around the kernel, as $\dot{M}_{\rm k} = 0.2\times10^{-6}\,{\rm M}_\odot\ {\rm yr}^{-1}$. In this case, the time-scale of a protostar formation can then be estimated as $t = M_{\rm k}/\dot{M}_{\rm k} \sim 2.0\times10^6$ yr, which is $\sim$13 times the infall time-scale estimated in Model III (Zhou et al. 1993).

4 CONCLUSIONS

We have investigated and analysed the effects of radial dynamical and thermal structures of an inside-out core collapsing cloud with spherical symmetry on forming molecular line profiles emitted from star-forming molecular clouds. A simple radiative transfer model employing a direct ray-tracing algorithm along the line of sight is constructed for computing H_2CO 140 GHz emission-line profiles in order to compare with those actually observed in a star-forming cloud. We model the gravitational core collapse of a molecular cloud by the self-similar hydrodynamics of a conventional polytropic gas under self-gravity in a self-consistent manner (Model I). We emphasize that an *isothermal* inside-out collapse model (Model II) cannot produce asymmetric molecular line profiles. In contrast, a variable radial temperature structure, which is crucial for determining asymmetric molecular line profiles, can be derived self-consistently together with the radial velocity and density structures in Model I, which is different from the semi-empirical approach (Model III). We explicitly demonstrate that Model I can indeed produce asymmetric double-peaked line profiles with stronger blue peaks than red peaks as observed in many star-forming molecular globules. We assess the relative importance of effects due to line-centre opacities, intrinsic linewidths and polytropic index γ in Model I. Our radiative transfer calculations further show that the presence of a dense static inner kernel around the centre of a core collapsing cloud gives a characteristic signature of a suppressed red wing of the blue line peak in the molecular line profile. We show an application to line-profile observations by modelling the 140 GHz H_2CO emission-line profile from the centre of the Bok molecular globule B335. We note that sensible fits to the H_2CO emission-line profile of B335 require a dense static kernel in addition to conditions of a polytropic core collapse model and an estimated line-of-sight receding speed of the entire molecular cloud. Using Model I and the molecular line-profile fits, we could estimate the protostellar mass, the mass inside the static condensed kernel, the mass accretion rate just outside the kernel radius and the time-scale of the protostar formation.

ACKNOWLEDGMENTS

This research was supported in part by Tsinghua Centre for Astrophysics (THCA), by the National Natural Science Foundation of China (NSFC) grants 10373009 and 10533020 at Tsinghua University, and by the Yangtze Endowment and the SRFDP 20050003088 and 200800030071 at Tsinghua University. The hospitality of Institut für Theoretische Physik und Astrophysik der Christian-Albrechts-Universität Kiel Germany and of International Center for Relativistic Astrophysics Network (ICRANet) Pescara, Italy, is gratefully acknowledged. KW thanks G. Sarty for comments.

REFERENCES

André P., Motte F., Bacmann A., 1999, ApJ, 513, L57
Belloche A., André P., Despois D., Blinder S., 2002, A&A, 393, 927
Bodenheimer P., Sweigart A., 1968, ApJ, 152, 515
Bonnor W., 1956, MNRAS, 116, 351
Cao Y., Lou Y.-Q., 2009, MNRAS, in press (arXiv:0908.3225)
Chandrasekhar S., 1960, Radiative Transfer. Dover Press, New York
Choi M., Evans N. J. II, Gregersen E. M., Wang Y., 1995, ApJ, 448, 742
De Vries C. H., Narayanan G., Snell R. L., 2002, ApJ, 577, 798
De Vries C. H., Myers P., 2005, ApJ, 620, 800
Dyson J. E., Williams D. A., 1997, The Physics of the Interstellar Medium, 2nd edn. IoP Publishing, Bristol
Ebert R., 1955, Z. Astrophys., 37, 217
Evans N. J. II, Rawlings J. M. C., Shirley Y. L., Mundy L. G., 2001, ApJ, 557, 193
Evans N. J. II, Lee J.-E., Rawlings J. M. C., Choi M., 2005, ApJ, 626, 919
Evans N. J. II, et al, 2009, ApJS, 181, 321
Fatuzzo M., Adams F. C., Myers P. C., 2004, ApJ, 615, 813
Frerking M. A., Langer W. D., Wilson R. W., 1987, ApJ, 313, 320
Gao Y., Lou Y.-Q., 2009, MNRAS, in press (arXiv:0909.1130)
Harvey D. W. A., Wilner D. J., Myers P. C., 2003, ApJ, 583, 809
Hogerheijde M. R., Sandell G., 2000, ApJ, 534, 880
Hu R.-Y., Lou Y.-Q., 2008, MNRAS, 390, 1619
Hunter C., 1977, ApJ, 218, 834
Keto E., Rybicki G. B., Bergin E. A., Plume R., 2004, ApJ, 613, 355
Larson R. B., 1969, MNRAS, 145, 271
Larson R. B., 1981, MNRAS, 194, 809
Lee J.-E., Bergin E. A., Evans N. J. II, 2004, ApJ, 617, 360
Li Z. Y., Nakamura F., 2006, ApJ, 640, L187
Lou Y.-Q., Cao Y., 2008, MNRAS, 384, 611
Lou Y.-Q., Gao Y., 2006, MNRAS, 373, 1610
Lou Y.-Q., Hu R. Y., 2009, New Astron., in press (arXiv:0905.3490)
Lou Y.-Q., Shen Y., 2004, MNRAS, 348, 717
Lou Y.-Q., Wang W.-G., 2006, MNRAS, 372, 885
Lou Y.-Q., Zhai X., 2009, Ap&SS, 323, 17
MacLow M.-M., 1999, ApJ, 524, 169
Mardones D., Myers P. C., Tafalla M., Wilner D. J., 1997, ApJ, 489, 719
Matzner C., 2007, ApJ, 659, 1394
Myers P. C., 2005, ApJ, 623, 280
Myers P. C., 2008, ApJ, 687, 340
Pavlyuchenkov Ya., Wiebe D., Shustov B., Henning Th., Launhardt R., Semenov D., 2008, ApJ, 689, 335
Penston M. V., 1969, MNRAS, 144, 425
Rawlings J. M. C., Yates J. A., 2001, MNRAS, 326, 1423
Rybicki G. B., Lightman A. P., 1979, Radiative Processes in Astrophysics. Wiley, New York
Saito M., Sunada K., Kawabe R., Kitamura Y., Hirano N., 1999, ApJ, 518, 334
Shen Y., Lou Y.-Q., 2004, ApJ, 611, L117
Shen Y., Lou Y.-Q., 2006, MNRAS, 370, L85
Shirley Y. L., Evans N. J. II, Rawlings J. M. C., 2002, ApJ, 575, 337
Shu F. H., 1977, ApJ, 214, 488
Shu F. H., Adams F. C., Lizano S., 1987, ARA&A, 25, 23
Snell R. L., 1981, ApJS, 45, 121
Stutz A. M. et al., 2008, ApJ, 687, 389
Suto Y., Silk J., 1988, ApJ, 326, 527
Tafalla M., Mardones D., Myers P. C., Caselli P., Bachiller R., Benson P. J., 1998, ApJ, 504, 900

Tafalla M., Myers P. C., Caselli P., Walmsley C. M., Comito C., 2002, ApJ, 569, 815
Tafalla M., Santiago J., Myers P. C., Caselli P., Walmsley C. M., Crapsi A., 2006, A&A, 455, 577
Tomita Y., Saito T., Ohtani H., 1979, PASJ, 31, 407
Tsai J. C., Hsu J. J. L., 1995, ApJ, 448, 774
Tsamis Y. G., Rawlings J. M. C., Yates J. A., Viti S., 2008, MNRAS, 388, 898
van der Tak F. F. S., Caselli P., Ceccarelli C., 2005, A&A, 439, 195
Wang W.-G., Lou Y.-Q., 2008, Ap&SS, 315, 135
Ward-Thompson D., Buckley H. D., 2001, MNRAS, 327, 955
Wilner D. J., Myers P. C., Mardone S., Tafalla M., 2000, ApJ, 544, L69
Yang J., Jiang Z., Wang M., Ju B., Wang H., 2002, ApJS, 141, 157
Zhou S., Evans N. J. II, Butner H. M., Kutner M. L., Leung C. M., Mundy L. G., 1990, ApJ, 363, 168
Zhou S., Evans N. J. II, Kömpe C., Walmsley C. M., 1993, ApJ, 404, 232

APPENDIX A: HYDRODYNAMICS OF A CONVENTIONAL POLYTROPIC GAS

For the hydrodynamics of a conventional polytropic gas model of spherical symmetry without diffusive effects, we use the basic non-linear fluid equations in spherical polar coordinates (r, θ, ϕ), namely

$$\frac{\partial \rho}{\partial t} + \frac{1}{r^2}\frac{\partial}{\partial r}(r^2 \rho u) = 0 \,, \tag{A1}$$

$$\frac{\partial u}{\partial t} + u\frac{\partial u}{\partial r} = -\frac{1}{\rho}\frac{\partial p}{\partial r} - \frac{GM}{r^2}, \tag{A2}$$

$$\frac{\partial M}{\partial t} + u\frac{\partial M}{\partial r} = 0 \,, \qquad \frac{\partial M}{\partial r} = 4\pi r^2 \rho. \tag{A3}$$

Here the mass density ρ, radial bulk flow velocity u, thermal pressure p and enclosed mass M are all functions of radius r and time t and $G = 6.67 \times 10^{-8}\,\mathrm{g^{-1}\,cm^3\,s^{-2}}$ is the gravitational constant. Equations (A1) and (A2) are the mass and radial momentum conservations, respectively; equation (A3) represents another form of mass conservation and the Poisson equation relating ρ to the gravitational potential Φ is consistently satisfied by the above equations.

The polytropic EoS reads

$$p = K(t)\rho^{\gamma}, \tag{A4}$$

where γ is the polytropic index and $K(t)$ is a coefficient. The self-similar dynamics involves an independent variable

$$x = r/(k^{1/2}t^n), \tag{A5}$$

where n is a scaling index and k is referred to as the sound parameter, and the corresponding self-similar transformation of other relevant hydrodynamic variables is

$$\rho = \frac{\alpha(x)}{(4\pi G t^2)}, \qquad M = \frac{k^{3/2}t^{3n-2}m(x)}{(3n-2)G},$$
$$u = k^{1/2}t^{n-1}v(x), \qquad p = kt^{2n-4}\alpha^{\gamma}(x)/(4\pi G), \tag{A6}$$

where $\alpha(x)$, $m(x)$ and $v(x)$ are dimensionless reduced mass density, enclosed mass and radial flow velocity, respectively. In reference to EoS (A4), we identify $K(t) \equiv k(4\pi G)^{\gamma-1}\, t^{2(\gamma+n-2)}$. For $n + \gamma = 2$, K becomes a constant for a conventional polytropic gas (e.g. Suto & Silk 1988; Lou & Gao 2006; Lou & Wang 2006; Hu & Lou 2008). The gas temperature T and the local polytropic sound speed c are

$$T \equiv \frac{\mu m_{\rm H}}{k_{\rm B}}\frac{p}{\rho} = \frac{\mu m_{\rm H}}{k_{\rm B}}\alpha^{\gamma-1}kt^{2n-2}, \tag{A7}$$

$$c \equiv (\partial p/\partial \rho)^{1/2} = (k\gamma)^{1/2}t^{n-1}\alpha^{(\gamma-1)/2}, \tag{A8}$$

where $k_{\rm B}$, μ and $m_{\rm H}$ represent the Boltzmann constant, mean molecular weight and the hydrogen mass, respectively. For typical star-forming clouds, we shall take $\mu \cong 1$ for simplicity. This self-similar transformation deals with an important subset of non-linear solutions to polytropic hydrodynamic partial differential equations (PDEs) (A1)−(A4) and provides the dynamic structures for radiative transfer calculations of molecular line profiles.

With self-similar transformation (A6) in non-linear PDEs (A1)–(A4), we obtain two coupled non-linear ordinary differential equations (ODEs):

$$[(v-nx)^2 - \gamma\alpha^{\gamma-1}]\frac{{\rm d}v}{{\rm d}x} = \frac{(v-nx)^2\alpha}{(3n-2)} + \frac{2(v-x)\gamma\alpha^{\gamma-1}}{x} - (v-nx)(n-1)v, \tag{A9}$$

$$[(v-nx)^2 - \gamma\alpha^{\gamma-1}]\frac{{\rm d}\alpha}{\alpha\,{\rm d}x} = (n-1)v - \frac{(v-nx)\alpha}{(3n-2)} - \frac{2(v-x)(v-nx)}{x}. \tag{A10}$$

By setting $v = 0$ for all $x > 0$, we obtain a static SPS from (equations (A9) and (A10):

$$v = 0, \qquad \alpha = [2\gamma(3n-2)/n^2]^{1/n}x^{-2/n},$$
$$m = (2\gamma)^{1/n}(3n-2)^{1/n}n^{-\gamma/n}x^{(4-3\gamma)/n}\,. \tag{A11}$$

To leading orders, asymptotic similarity solutions of coupled non-linear ODEs (A9) and (A10) for $x \to +\infty$ and $x \to 0^+$ are summarized below. In the limit of $x \to +\infty$, we have

$$\alpha = Ax^{-2/n}, \qquad v = -\frac{nA}{(3n-2)}x^{(n-2)/n} + \frac{2\gamma A^{\gamma-1}}{n}x^{(2-2\gamma-n)/n} + Bx^{(n-1)/n}, \tag{A12}$$

where A and B are two constants of integration. In asymptotic solution (A12), it is possible to set $B = 0$ with a finite $A > 0$ such that v vanishes at large x, and this A is precisely the coefficient of $\alpha(x)$ in SPS solution (A11). This consistency is expected but SPS solution (A11) is valid for all x except for the central singularity. In the limit of $x \to 0^+$, the asymptotic central free-fall solution is

$$v = -\left[\frac{2m_0}{(3n-2)x}\right]^{1/2}, \qquad \alpha = \left[\frac{(3n-2)m_0}{2x^3}\right]^{1/2}, \tag{A13}$$

where $m = m_0$ is the reduced enclosed mass $m(x) = \alpha x^2(nx - v)$ as $x \to 0^+$, for a point mass at the centre.

By free-fall solution (A13) and transformation (A6) with $n + \gamma = 2$, we have a variable central mass accretion rate $\dot{M}$ given by

$$\dot{M} = k^{3/2}t^{(3-3\gamma)}m_0/G. \tag{A14}$$

Only for the isothermal case of $\gamma = 1$ $(n = 1)$ can we have a constant $\dot{M}$. We solve non-linear ODEs (A9) and (A10) numerically using the fourth-order Runge–Kutta method. The SPS solution (A11) and asymptotic conditions (A12) and (A13) are all used to determine self-similar dynamic flows. We also pay attention to the sonic critical curve (see Lou & Gao 2006; Gao & Lou 2009; Lou & Wang 2006; Hu & Lou 2008 for details).

APPENDIX B: FORMATION OF DOUBLE-PEAK MOLECULAR LINE PROFILES

Extensive spectral observations often show two peaks in high excitation emission molecular line profiles from star-forming molecular

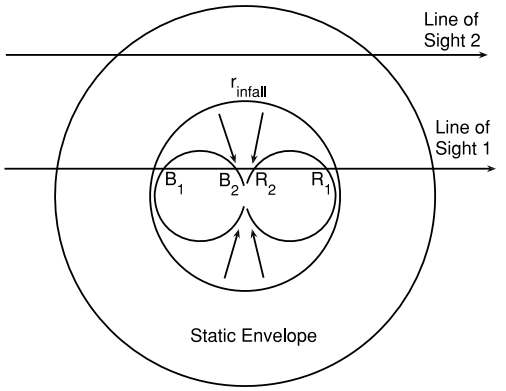

Figure B1. A schematic illustration of the inside-out collapse scenario for the formation of double-peaked molecular line profiles. The cloud consists of an outer static envelope and an inner collapsing core, separated by a spherical surface at $r = r_{\rm infall}$ in radial expansion. The loci (i.e. the two connected ovals) of a particularly chosen constant projected line-of-sight velocity component are shown. Two lines of sight are drawn towards right, labelled by 'Line of Sight 1' and 'Line of Sight 2', respectively. Line of Sight 1 passes through the core of central infall as well as the outer static envelope, that intercepts the ovals at points B_1 and B_2 for the same approaching projected velocity components and at points R_1 and R_2 for the same receding projected velocity components. Sufficiently far away from the centre, Line of Sight 2 passes through only the outer static envelope.

globules, and the blue peak is usually stronger than the red peak (i.e. blue asymmetric lines). This phenomenon can be explained in the framework of the inside-out collapse model (Shu 1977). We recount below the relevant molecular line-profile formation processes (Zhou et al. 1993).

Consider a spherically symmetric and non-rotating molecular cloud. In the isothermal inside-out collapse model of Shu (1977), the cloud consists of two radial regions, namely (i) an inner collapsing core and (ii) an outer static envelope, as depicted in Fig. B1. For simplicity, we use a static envelope here. The dynamical infall at the inner region determines the velocity profiles and hence the families of loci with equal magnitudes of projected line-of-sight velocity components. In Fig. B1, we show two loci of the families that have equal magnitudes of projected line-of-sight velocity components but opposite directions. In the limit of no absorption (i.e. the optically thin regime), molecular lines from the emitters on these two loci will split, forming two symmetric components of peaks with equal but opposite (blue and red) frequency shifts.

Let us first pick up Line of Sight 2 which passes through only the outer static envelope. This is a simple situation that the line has no bulk velocity broadening and splitting, i.e. a single-peaked line profile characterized by thermal and microscopic turbulence broadenings would be expected. Next, we consider Line of Sight 1 which passes through both the outer static envelope and the infalling core. Line of Sight 1 intercepts the two loci of each family of constant projected velocity component at four points, namely B_1, B_2, R_1 and R_2, with B and R implicating blue and red shifts, respectively. We may denote the intensities of emission-line components at these blue and red shifts as $I_{\rm blue}$ and $I_{\rm red}$. Suppose that the absorption of the emission line by the continuum is insignificant in the collapsing core. For illustration here, we may ignore the extinction in the envelope without losing generality, as it introduces only a scaling factor equally applied to both $I_{\rm blue}$ and $I_{\rm red}$. With this simplification, the emission intensities are given by two transfer equations:

$$I_{\rm blue} = S_1(1 - {\rm e}^{-\tau_1}){\rm e}^{-\tau_2} + S_2(1 - {\rm e}^{-\tau_2}), \tag{B1}$$

$$I_{\rm red} = S_2(1 - {\rm e}^{-\tau_2}){\rm e}^{-\tau_1} + S_1(1 - {\rm e}^{-\tau_1}) \tag{B2}$$

(e.g. Zhou et al. 1993), where in the vicinity of points 1 and 2, τ_1 and τ_2 are the optical depths, while S_1 and S_2 are the source functions, with subscripts 1 and 2 denoting the outer and inner portions, respectively, within the collapsing core at which four points (B_1, R_1) and (B_2, R_2) are located. It follows that the difference between the blue and red components of the line at this projected velocity component is

$$I_{\rm blue} - I_{\rm red} = (S_2 - S_1)(1 - {\rm e}^{-\tau_2})(1 - {\rm e}^{-\tau_1}). \tag{B3}$$

For a local thermal equilibrium (LTE), the source function S is given by the local Planck function (e.g. Rybicki & Lightman 1979). In the Rayleigh–Jeans regime of lower frequencies, the spectral intensity I_ν may be expressed in terms of the brightness temperature $T_{\rm b}$ in the form of $I_\nu = 2\nu^2 k_{\rm B} T_{\rm b}/c^2$, where ν, c and $k_{\rm B}$ are the frequency, the speed of light and the Boltzmann constant, respectively (e.g. Dyson & Williams 1997). Hence, the difference in brightness temperatures between the blue and red peak emissions of a molecular line profile is simply

$$T_{\rm b,blue} - T_{\rm b,red} = (T_2 - T_1)(1 - {\rm e}^{-\tau_2})(1 - {\rm e}^{-\tau_1}). \tag{B4}$$

Equation (B4) shows that a maximum contrast in the two peaks happens in the regimes of $\tau_1 \gg 1$ and $\tau_2 \gg 1$, and this gives a brightness temperature peak difference $T_{\rm blue} - T_{\rm red} \approx T_2 - T_1$. Asymmetric line profiles arise only when there are substantial line optical depths in the hemispheres of the collapsing core that give rise to blue and red shifts of the line. In the opposite regimes of $\tau_1 \ll 1$ and $\tau_2 \ll 1$, the brightness temperature peak difference becomes $T_{\rm blue} - T_{\rm red} \approx (T_2 - T_1)\tau_1\tau_2 \approx 0$. In this case, the equal strengths of the two peaks can be understood as a direct consequence where in the absence of absorption (i.e. an optically thin gas) the emission from any location along the line of sight is visible.

Molecular emission lines commonly used for cloud structure diagnostics (e.g. molecules H_2CO, HCO^+, CS, N_2H^+ etc; see Zhou, Evans & Butner 1990; Zhou et al. 1993; Dyson & Williams 1997; Ward-Thompson & Buckley 2001; Lee, Bergin & Evans 2004; Tsamis et al. 2008) are opaque in molecular globules that form protostars. For a collapsing core under the self-gravity, an increase in the temperature towards the centre, i.e. $T_2 > T_1$, would then lead to a stronger blue peak than the red peak in the emission-line profile. The observed stronger blue peaks in the H_2CO and CS line profiles from the molecular globule B335 thus support the notion of a collapsing core and, in particular, the inside-out collapse scenario. But such clouds cannot be isothermal. Moreover, the temperature should be higher towards the cloud centre.

APPENDIX C: RADIATIVE TRANSFER CALCULATIONS OF MOLECULAR LINES

The ray-tracing radiative transfer equation in the LTE approximation reads

$$\frac{{\rm d}}{{\rm d}s} I_\nu = -(\kappa_{\rm c} + \kappa_{\rm l})\rho I_\nu + \kappa_{\rm c}\rho S_{\rm c} + \kappa_{\rm l}\rho S_{\rm l} \tag{C1}$$

(e.g. Chandrasekhar 1960) where ds is the ray path differential element, ρ is the mass density, $S_{\rm c}$ and $S_{\rm l}$ are the source functions, $\kappa_{\rm c}$ and $\kappa_{\rm l}$ are the mass absorption coefficients (or opacities), and the subscripts 'c' and 'l' refer to associations with the continuum and line emissions, respectively. The corresponding optical depths are defined by

$$\tau_{\rm c} = \int_0^s {\rm d}s' \rho\kappa_{\rm c}(s') \qquad \text{and} \qquad \tau_{\rm l} = \int_0^s {\rm d}s' \rho\kappa_{\rm l}(s'). \tag{C2}$$

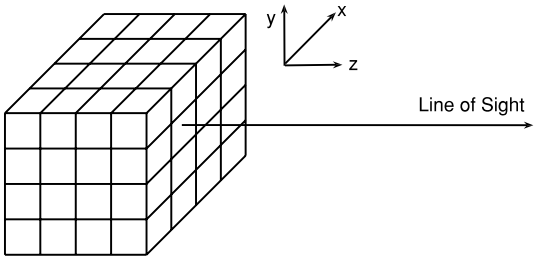

Figure C1. An illustration of the computational grid in our ray-tracing radiative transfer calculations (with $4^3 = 64$ cubic cells). The intensity of a molecular line is calculated cell by cell sequentially along each ray parallel to the z-axis. The spectral image is formed in the (x, y) plane of the sky. In our calculations for molecular emission-line profiles, typically 101^3 cubic cells are used.

For spectral line emissions, the opacity takes the form of $\kappa_\mathrm{l} = \kappa_{\mathrm{l}_0}\phi_\nu$, where κ_{l_0} is the line-centre opacity and dimensionless ϕ_ν is the normalized spectral line-profile function in radiation frequency ν. The continuum remains more or less constant in the narrow frequency range of a spectral line profile; thus a molecular line profile is mainly determined by the opacity, source function and the intrinsic line-profile function ϕ_ν. For simplicity, we ignore continuum contributions by setting $\kappa_\mathrm{c} = 0$ and $S_\mathrm{c} = 0$ at this stage. Hereafter and in the main text, the subscript 'l' is also suppressed.

To solve radiative transfer equation (C1), we apply a forward ray-tracing computational algorithm on a three-dimensional (3D) Cartesian (x, y, z) grid with N^3 cells with N being the number of grids along each side. A spherical molecular cloud is embedded inside such a cubic grid. A ray propagates parallel to the z-direction towards an observer and the spectral image of a cloud is projected on to the (x, y) plane of sky perpendicular to the z-direction (see Fig. C1). We use $N^3 = 101^3$ cubic cells with an equal edge length of Δs for each grid cell which provide a sufficient spatial resolution for the purpose of our line-profile computations.

Approximately, each cell is locally homogeneous in density, temperature and velocity, with their values taking the local values of a model molecular cloud at the cell centre. The numerical difference scheme for the local solution to transfer equation (C1) in a cell can be cast as

$$I_n = I_{n-1}\mathrm{e}^{-\Delta\tau_n} + S_n(1 - \mathrm{e}^{-\Delta\tau_n}), \tag{C3}$$

where I_n is the emerging emission from the nth cell, and S_n and $\Delta\tau_n$ are the source function and the optical depth of the nth cell, respectively. By equation (C2), the optical depth of the nth cell is

$$\Delta\tau_n = \rho\kappa\Delta s = \rho\kappa_0\phi(v,\ v_\mathrm{p})\Delta s, \tag{C4}$$

where ρ is the mass density of the cell, κ is the effective line opacity, κ_0 is the line-centre opacity and $\phi(v, v_\mathrm{p})$ is the intrinsic-normalized line profile. $\phi(v,\ v_\mathrm{p})$ in equation (C4) is a function of velocity components v and v_p, which correspond to the emission frequency ν and the gas velocity in the cell projected along the line of sight, respectively. We assume for simplicity that molecular line profiles are intrinsically Gaussian with a normalized line-profile function in the form of

$$\phi_\nu \rightarrow \phi(v,\ v_\mathrm{p}) = (2\pi\,\Delta v^2)^{-1/2}\exp\left[-\frac{(v - v_\mathrm{p})^2}{2\Delta v^2}\right], \tag{C5}$$

where v_p is the velocity component of the emitter projected along the line of sight and Δv^2 is the square of the 'intrinsic' characteristic broadening of a tracer molecular line in the absence of large-scale systematic dynamic flows. This intrinsic broadening includes both the thermal and the micro-turbulence effects. The source function of the nth cell is given by the local Planck function $(2h\nu^3/c^2)\{\exp[h\nu/(k_\mathrm{B}\ T)] - 1\}^{-1}$ where h is the Planck constant. For emission lines in the Rayleigh–Jeans regime of low frequencies, we then have $S_n = 2\nu^2 k_\mathrm{B} T/c^2$, where T is the thermal temperature of the cell.

Our radiative transfer calculations are first carried out in a cell for a fixed frequency ν and proceed sequentially to the adjacent cell along a ray parallel to the z-direction. Such calculations are then repeated for a range of frequencies along the same ray path. After finishing the integration along a ray, the same procedure will be repeated for all other rays on the grid, which then generates a molecular line spectrum for each spatial pixel on the image plane. Depending on the desired spatial resolution, summation over the spectra of relevant pixels would give a line spectrum from a part of a molecular cloud.

This paper has been typeset from a TEX/LATEX file prepared by the author.